Electronic supplementary information

Bioinspired Electrocatalyst for CO_2 Electroreduction to Ethanol via Secondary-Sphere Synergy in Fe Porphyrinic-Based Metal-Organic Frameworks

Kaian Sun,[a] Shaohui Xie,[a] Ping Guan,[a] Zewen Zhuang,[a] Xin Tan,[a] Wei Yan,*[a] Jiujun Zhang*[a] and Chen Chen*[b]

[a] Institute of New Energy Materials and Engineering, Fujian Engineering Research Center of High Energy Batteries and New Energy Equipment & Systems, School of Materials Science and Engineering, Fuzhou University, Fuzhou 350108, P. R. China.

[b] Engineering Research Center of Advanced Rare Earth Materials, Department of Chemistry, Tsinghua University, Beijing 100084, P. R. China.

E-mail: weiyan@fzu.edu.cn; jiujun.zhang@fzu.edu.cn; cchen@mail.tsinghua.edu.cn

Table of Contents

1. Experimental Details

1.1 Materials

Commercial carbon black XC-72R, N,N-Dimethylformamide (99.9%, DMF), zirconyl chloride octahydrate (99.9%, $ZrOCl_2 \bullet 8H_2O$), and acetic acid (99.9%, AA) were purchased from Innochem Co., Ltd. 5-Benzimidazolecarboxylic acid (BAA) was purchased from Tci., Ltd. Acetone was purchased from Sinopharm Chemical Reagent Co.,Ltd. 5,10,15,20-tetrakis(4-carboxyphenyl)porphyrin Fe (II) (95%, FeTCPP), 5,10,15,20-Tetrakis(4-hydroxyphenyl)porphyrin (95%, TCPP), and 4,4,4,-Benzene-1,3,5-triyl-tris(benzoic acid) (95%, H_3BTB) were purchased from Jilin Chinese Academy of Sciences-Yanshen Technology Co., Ltd. Ultrapure water (>18 MΩ) obtained from a Milli-Q system was used throughout all the experiments. All gases were obtained from Linde Co., Ltd.

1.2. Syntheses

Synthesis of FeTCPP-NSs

7 mg of FeTCPP and 10 mg of BTB were dissolved in 7 mL of DMF under magnetic stirring for 15 min, and the resulting solution was labeled as Solution A. Separately, 30 mg of $ZrOCl_2 \bullet 8H_2O$, 2.2 mL of AA, and 2 mL of DMF were added to a 20 mL glass vial, followed by magnetic stirring for 15 min to prepare Solution B. Solution B was then heated at 120 °C for 1 h. After cooling to room temperature, Solution A was added to Solution B. The combined solution (A + B) was ultrasonically dispersed for 10 min and subsequently heated at 120 °C for 24 h. The resulting dark purple powder was collected via vacuum filtration and washed several times with DMF and acetone. Finally, the product was dried in a vacuum at 70 °C for 12 h to obtain FeTCPP-NSs.

Synthesis of TCPP-NSs

The synthesis method of TCPP-NSs is identical to that of FeTCPP-NSs, with the only difference being the substitution of TCPP for FeTCPP.

Synthesis of FeTCPP-NSs-BAA

3 mg of BAA was dissolved in 10 mL of DMF under magnetic stirring for 15 min. Subsequently, 15 mg of FeTCPP-NSs was added to the clear solution, followed by ultrasonication for 30 min. The mixture was then heated at 120 °C for 12 h. The resulting precipitate was washed with DMF and acetone and dried under vacuum at 70 °C for 12 h to obtain FeTCPP-NSs-BAA.

1.3. Characterizations

Powder X-ray diffraction (PXRD) patterns were obtained using a Bruker D8 Advance XRD powder diffractometer with Cu Kα radiation. Electron paramagnetic resonance (EPR) measurements were made with a Bruker Elexsys model E500 spectrometer. Transmission electron microscopy (TEM) was conducted on an FEI Talos F200i field emission scanning transmission electron microscope with an accelerating voltage of 200 kV. N_2 and CO_2 sorption experiments were carried out at −196 and 0 °C on an ASAP 2460 instrument, respectively. H_2O sorption experiments were carried out at 25 °C on a Belsorp Max instrument. Fourier-transform infrared (FTIR) spectra were recorded on an iS50 spectrometer. X-ray photoelectron spectroscopy (XPS) was performed on a ULVAC PHI Quantera microscope. The binding energies were calibrated by C1s at 284.8 eV. The Fe K-edge XAFS spectra were collected at the BL20U beamline of the Shanghai Synchrotron Radiation Facility (SSRF). A home-made organic glass electrochemical cell was employed for the in situ X-ray absorption spectroscopy (XAS) characterizations. Data were collected in fluorescence mode using a Lytle detector, while the corresponding reference samples were collected in transmission mode. The acquired EXAFS data were processed using standard procedures with the ATHENA module of the Demeter software packages.[1,2] Thermogravimetric analyses (TG) were performed on a Q600 SDT instrument under a flow of N_2. In situ Raman measurements were conducted on a HORIBA LabRAM HR Evolution spectroscopy system with a 633 nm excitation laser beam (5%), using a three-electrode electrochemical cell equipped with a sapphire observation window (Beijing Zhongyan Huanke Technology Co., Ltd). For each measurement, the Raman spectrum was obtained 1 min after the potential was applied and accumulated through 6 acquisitions (30 s per acquisition). The attenuated total reflectance surface-enhanced infrared absorption spectroscopy experiments were taken with Nicolet iS50 FT-IR spectrometer equipped with an MCT detector cooled with liquid nitrogen and PIKE VeeMAX III variable angle ATR sampling accessory. The spectral resolution

was set to 4 cm^{-1} and 64 interferograms were co-added for each spectrum. A 60° Si face-angled crystal was used as reflection element. The ultra-thin Au film was deposited chemically in Si crystal for IR-signal enhancement and conduction of electrons. The electrocatalyst was dropped onto Au film to serve as a working electrode. The gas products of electrolysis were detected using a Shimadzu 2014 gas chromatograph equipped with TCD and FID detectors. The liquid products of electrolysis were analyzed using an Avance NEO 600 spectrometer (600 MHz ^1H frequency) with H_2O suppression.

1.4. Electrochemical measurements

All electrochemical tests were performed using a typical three-electrode setup, which includes a working electrode, a counter electrode (Pt sheet for H-cell and flow cell test, IrO_2-coated titanium mesh for membrane electrode assembly system test), and a reference electrode (3.0 M KCl Ag/AgCl). To prepare the electrocatalyst ink for the working electrode, 5 mg of the as-synthsized electrocatalysts and 5 mg XC-72R (as conductive additive) were added into a mixture of 1.5 mL isopropanol, 0.5 mL water, and 20 µL Nafion D-520 solution (5 wt%), which was then ultrasonicated for 30 min. 0.1 M $KHCO_3$ aqueous solution was obtained by bubbling CO_2 (99.99%) into a 0.05 M K_2CO_3 solution overnight and treated with Chelex 100 chelating resin. The catholyte in acidic condition consisted of a 0.5 M K_2SO_4 solution with the pH adjusted to 3 by adding 0.05 M H_2SO_4, monitored using a pH meter.

Electrochemical performance in an H-cell was tested at room temperature using a Chenhua CHI 760E electrochemical workstation. A Nafion 117 membrane was inserted between the cathodic and anodic chambers. Before the electrochemical measurements, the electrolytes were pre-electrolyzed overnight to further remove metal impurities and then saturated with high-purity CO_2 by purging CO_2 into the electrolytes for 30 min. 20 mL of the purified CO_2-saturated electrolyte was added to both the cathodic and anodic chambers, maintaining a CO_2 flow rate of 20 mL min^{-1} in the cathode chamber. When preparing the working electrode, 80 µL of the prepared ink was dropped onto a gas diffusion carbon paper (YLS-30T, working area of 0.5 cm^{-2}) and dried under an infrared lamp.

Electrochemical measurements in a flow cell were conducted at room temperature using an Autolab M204 electrochemical workstation with a commercial electrochemical cell (Gaosunion 101017-1.2 mm). Both the catholyte and anolyte were circulated using a peristaltic pump at a flow rate of 15 mL min^{-1}. The ink was sprayed onto a YSL-30T to serve as the working electrode (working area of 0.5 × 1.0 cm, loading mass of 1.0 mg cm^{-2}). The Nafion 117 membranes were used to separate the cathodic and anodic chambers in acidic condition tests. In the gas chamber, a CO_2 flow rate of 15 mL min^{-1} was maintained.

Note: In this work, statistical analysis was performed on the data of Faradaic efficiency and current density. All data were conducted by three independent tests and presented as the standard deviation.

1.5. Theoretical calculation

Electronic structure calculations were performed by plane-wave-based code Vienna ab initio simulation packages (VASP, version 5.4.4), with in density functional theory (DFT) framework.[3] The Perdew, Burke, and Ernzerhof (PBE) functional was adopted to express the exchange and correlation interactions.[4] The cutoff energy of the plane-wave basis is 450 eV. The Gaussian smearing function was employed to improve the convergence of states near the Fermi level with a smearing width of 0.05 eV. The long-range dispersion correction was incorporated within the PBE using Grimme's D3 dispersion correction (PBE + D3).[5] Spin polarization is included in the calculations. All atoms were fully relaxed in all dimensions till all residual forces have declined below 0.02 eV $Å^{-1}$ and the convergence of energy and forces were set to 1×10^{-5} eV. The Brillouin zone was sampled using the 1 × 1 × 1 Monkhorst-Pack sampling in structure optimization and the vacuum thickness was set to be 25 Å. Kinetic barriers are obtained using climbing-image nudged elastic band (CI-NEB).

2. Electronic supplementary figures

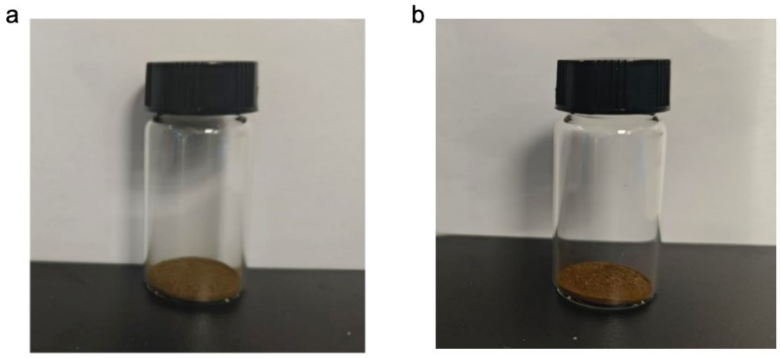

Fig. S1. Digital photographs of (a) FeTCPP-NSs and (b) FeTCPP-NSs-BAA.

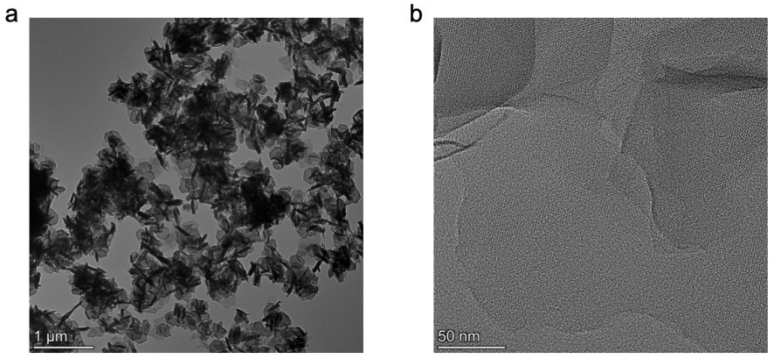

Fig. S2. (a) TEM and (b) HRTEM images of FeTCPP-NSs.

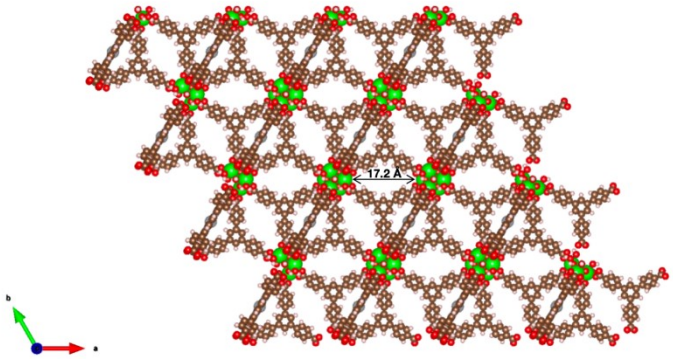

Fig. S3. The crystal model of FeTCPP-NSs.

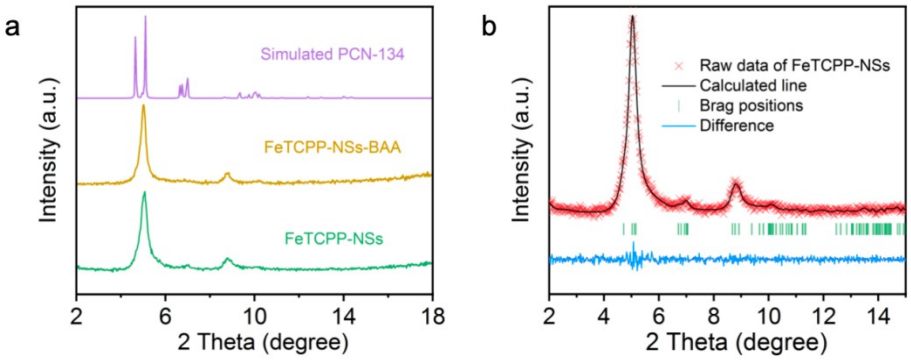

Fig. S4. (a) The XRD patterns of FeTCPP-NSs, FeTCPP-NSs-BAA, and simulated PCN-134 MOF. (b) Rietveld refinement of FeTCP-NSs against XRD data using the simulated PCN-134 MOF structure as reference.

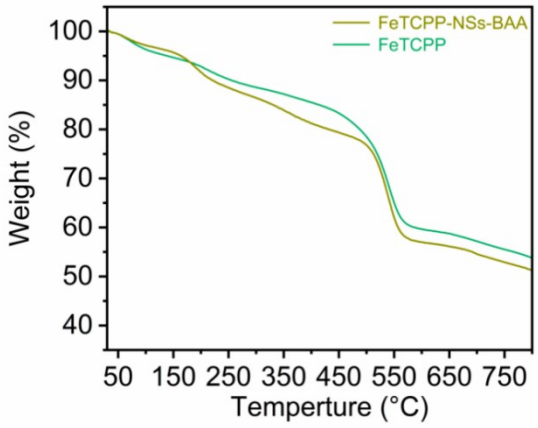

Fig. S5. Thermogravimetric analysis.

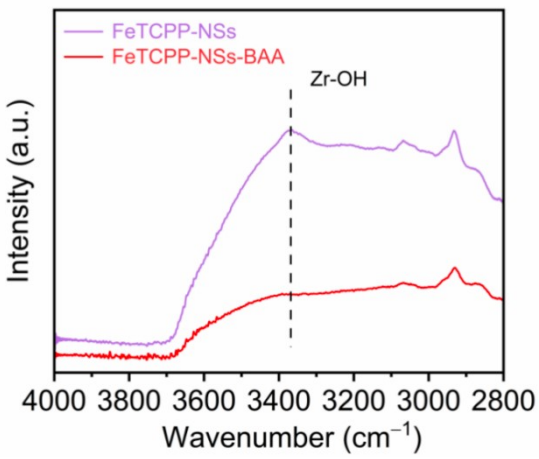

Fig. S6. The IR spectra.

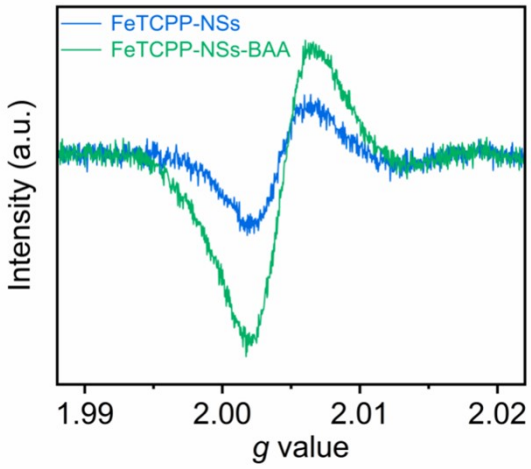

Fig. S7. The EPR pattern.

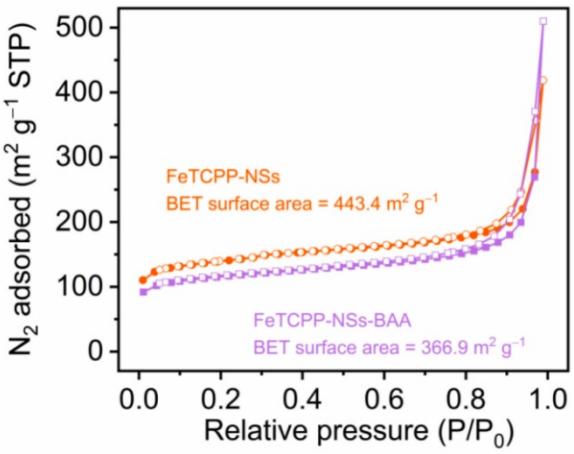

Fig. S8. The N_2 adsorption isotherms of FeTCPP-NSs and FeTCPP-NSs-BAA.

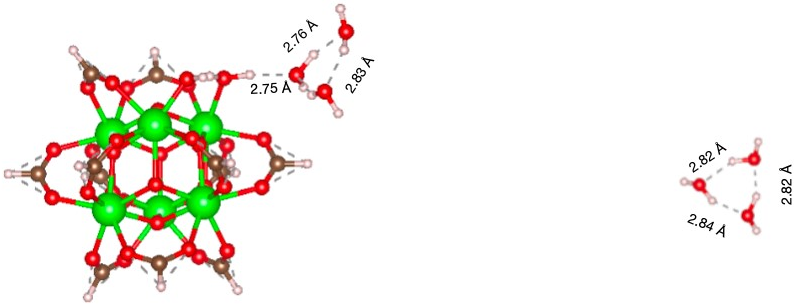

Fig. S9. The optimized adsorption model of H_2O moleculers surronding Zr_6 culsters and H_2O moleculers without Zr_6 culsters by DFT calculaitons.

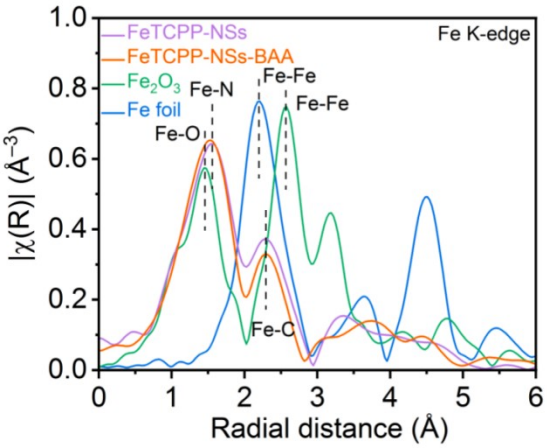

Fig. S10. Fe K-edge FT-EXAFS spectra in the R-space of FeTCPP-NSs, FeTCPP-NSs-BAA, Fe foil and Fe_2O_3 foil.

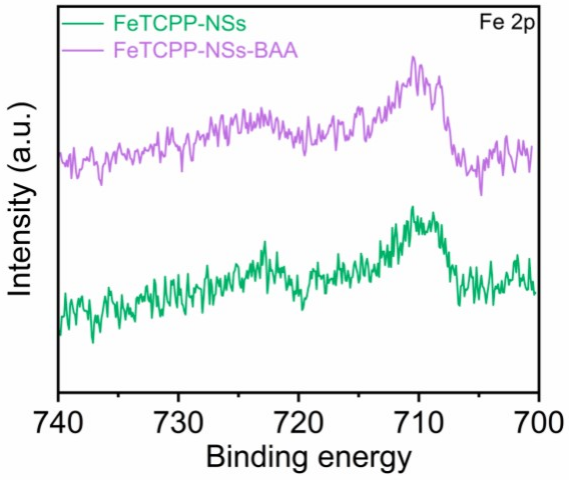

Fig. S11. The XPS pattern.

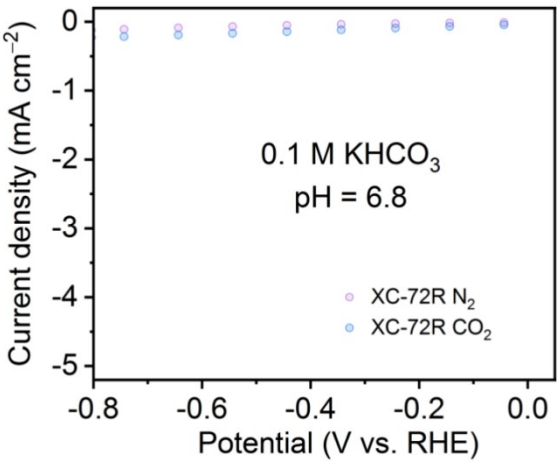

Fig. S12. LSV curves of carbon black measured in H-cell under neutral conditions. XC-72R exhibits negligible electrochemical activity toward CO_2RR, confirmming that the observed catalytic performances of FeTCPP-NSs-BAA, FeTCPP-NSs, and FeTCPP originate from the active catalyst itself rather than from the carbon black additive.

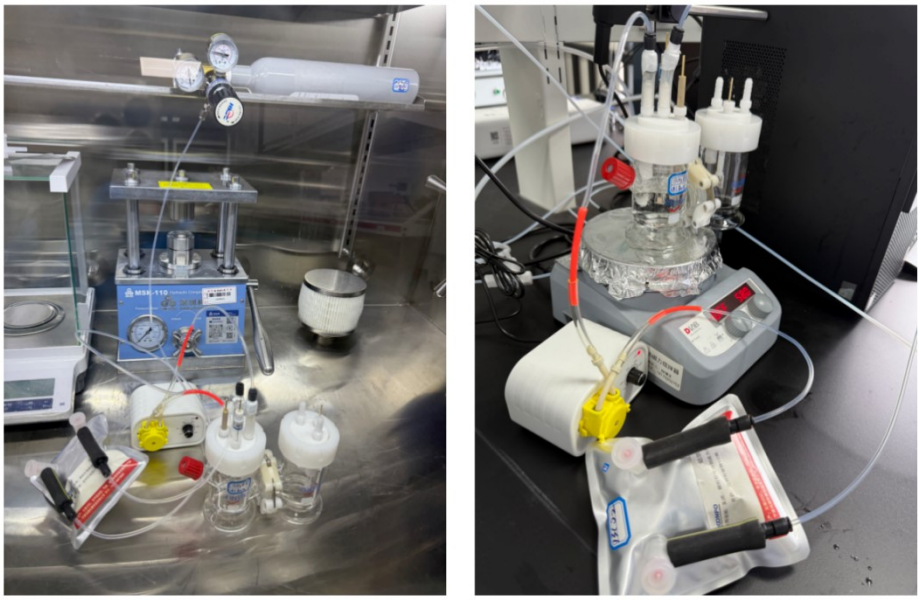

Fig. S13. The $^{13}CO_2$ isotope-labeling experiments.

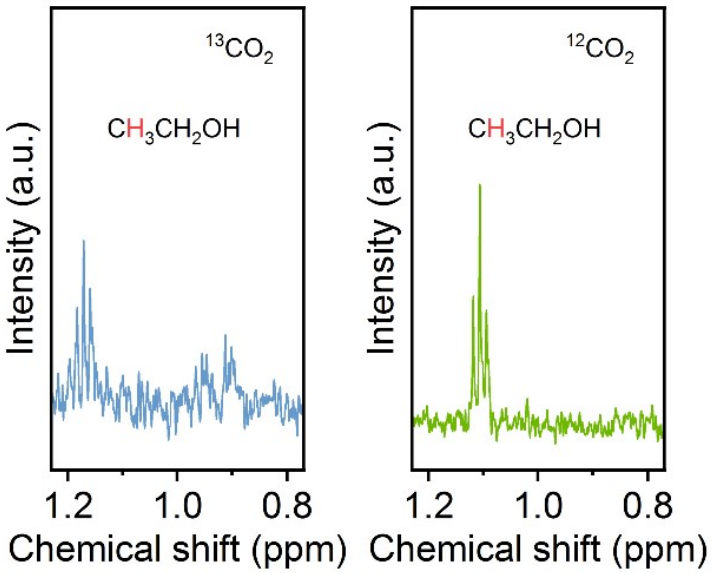

Fig. S14. The ^{1}H-NMR pattern.

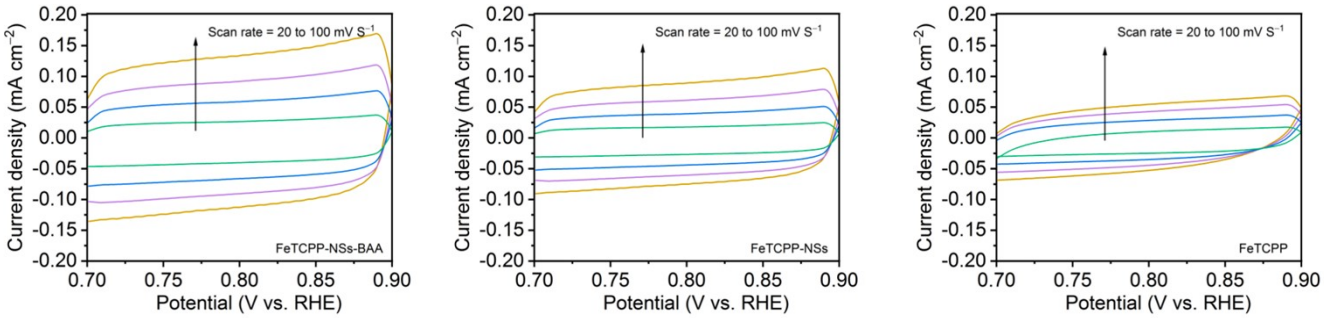

Fig. S15. The ECSA pattern.

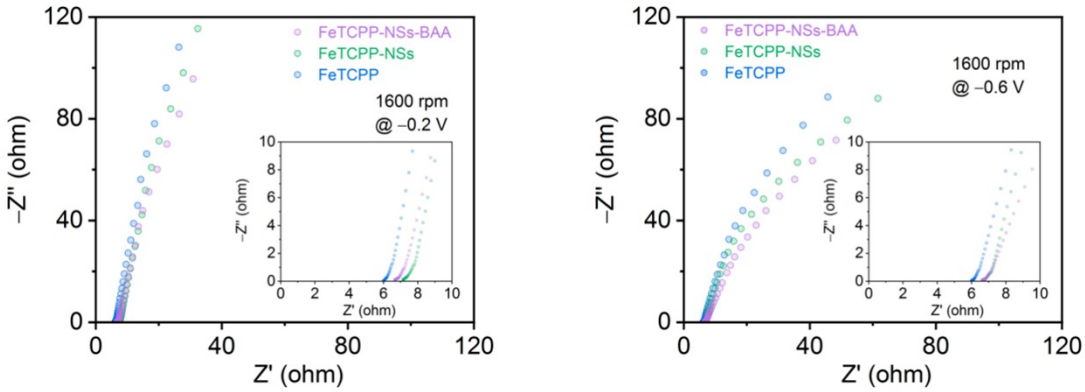

Fig. S16. The ECSA pattern under different applied potentials using a rotating disk electrode. The Nyquist plots reveal that at more negative potentials, the low frequencies become more pronounced for all samples, confirming that the low frequencies are associated with mass-transport resistance. Among the tested materials, FeTCPP-NSs-BAA exhibits the lowest mass-transport resistance compared to FeTCPP and FeTCPP-NSs.

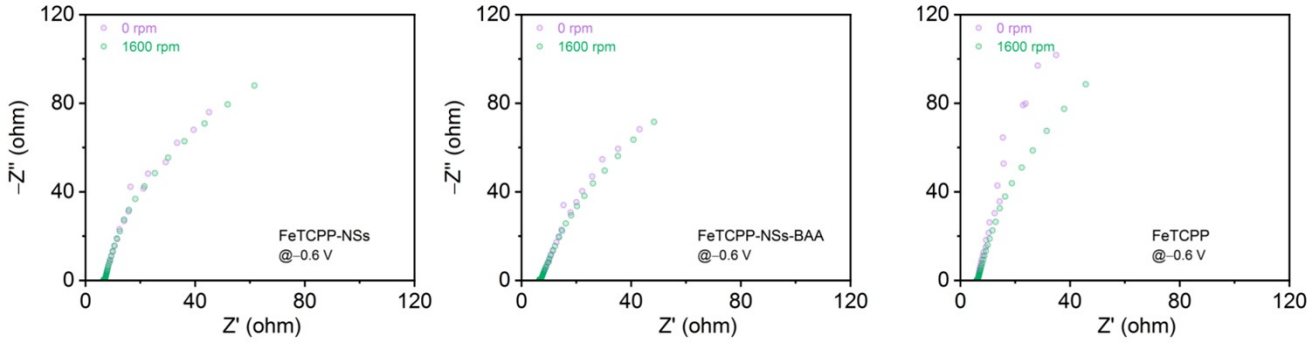

Fig. S17. The ECSA pattern under different rotation speeds using a rotating disk electrode. When the rotation rate was decreased from 1600 to 0 rpm, the increase in mass-transport resistance is minimal for FeTCPP-NSs and FeTCPP-NSs-BAA, whereas a significant increase can be found for FeTCPP.

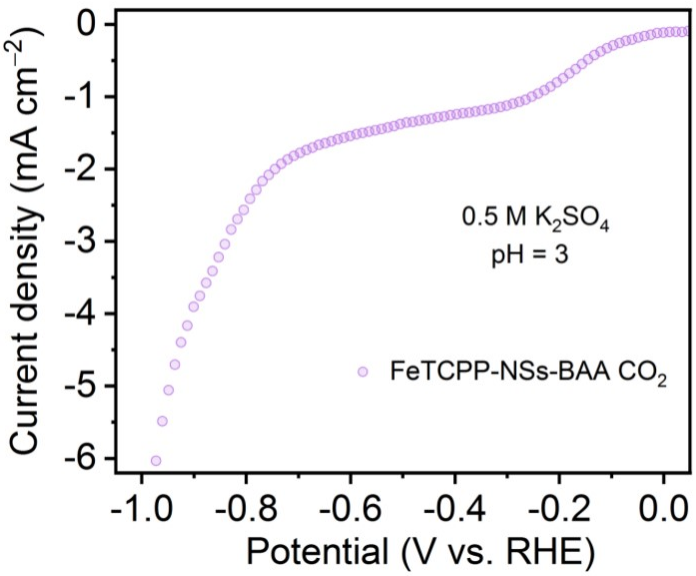

Fig. S18. The LSV curves measured in H cell under acidic conditions.

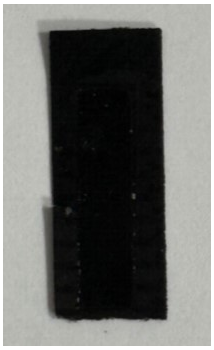

Fig. S19. The digital photographs of the gas diffusion electrode after 25 h of operation under acidic conditions.

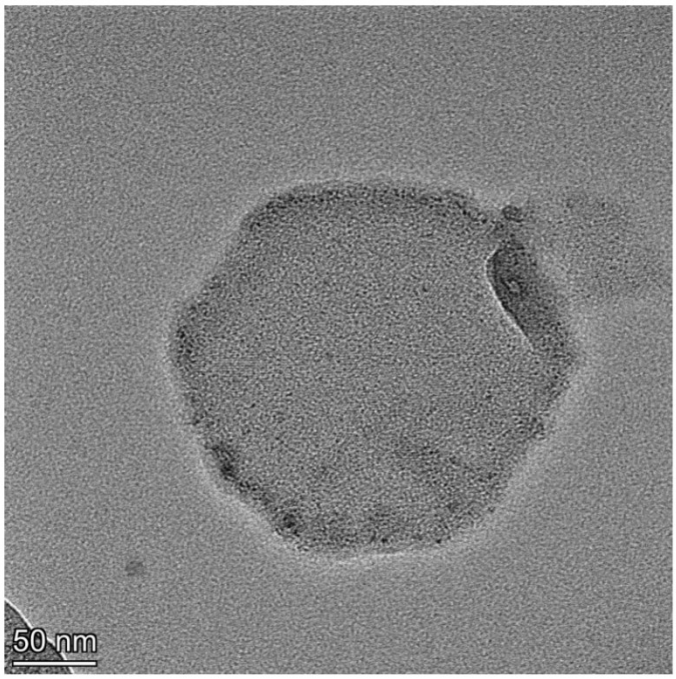

Fig. S20. The TEM images of used FeTCPP-NSs-BAA.

Fig. S21. The low-concentration CO_2 gas supply system.

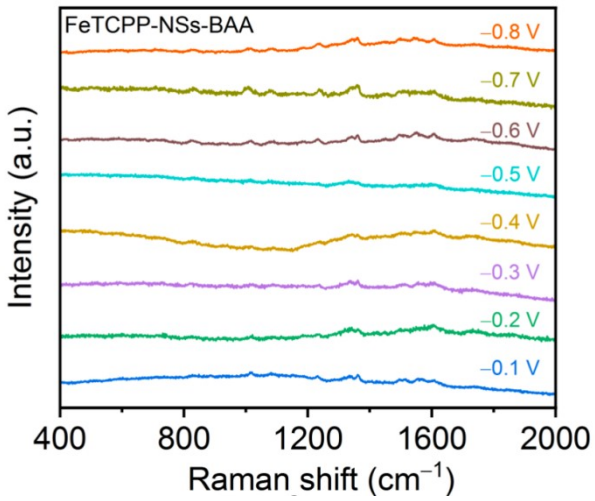

Fig. S22. Potential-dependent in situ Raman spectra.

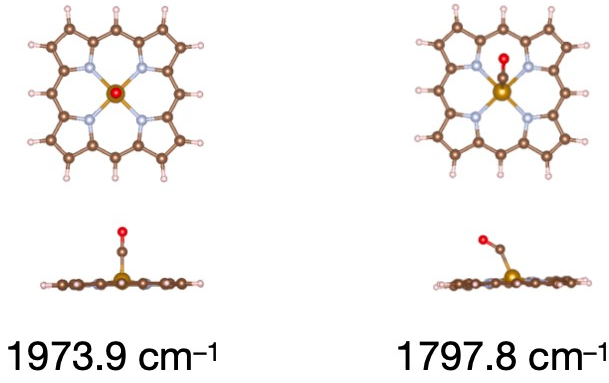

Fig. S23. IR frequencies derived from DFT calculations.

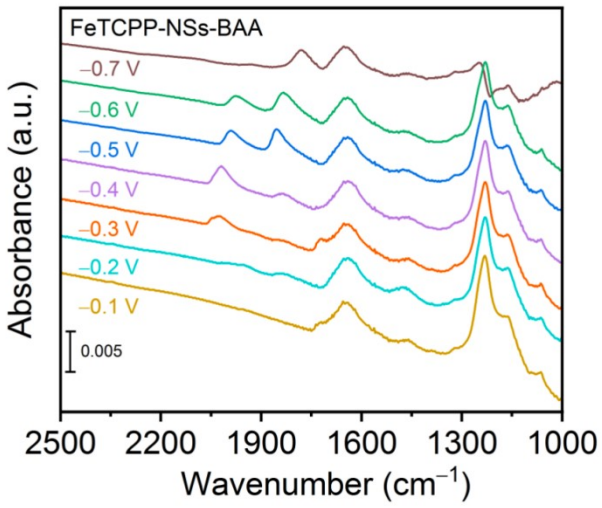

Fig. S24. Potential-dependent in situ ATR-SEIRAS spectra of FeTCPP-NS-BAA from –0.7 to –0.1 V.

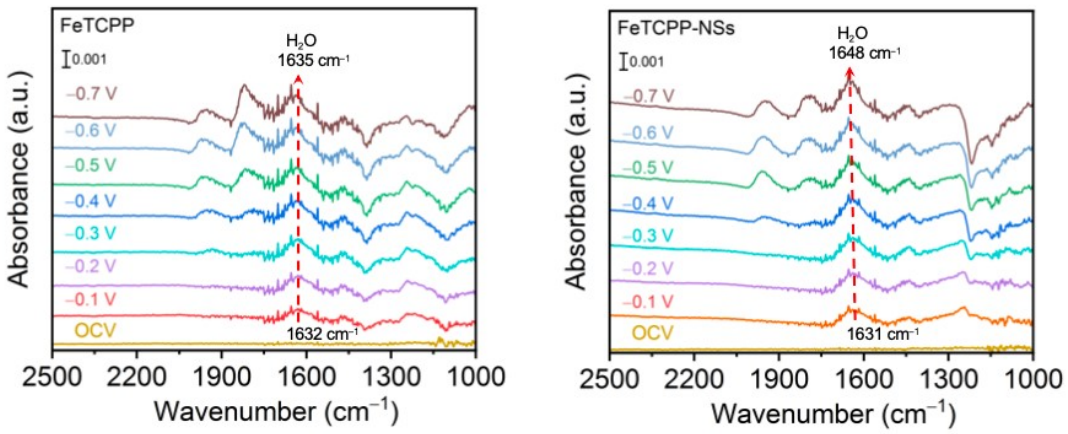

Fig. S25. Potential-dependent in situ ATR-SEIRAS spectra of FeTCPP and FeTCPP-NSs from –0.1 to –0.7 V.

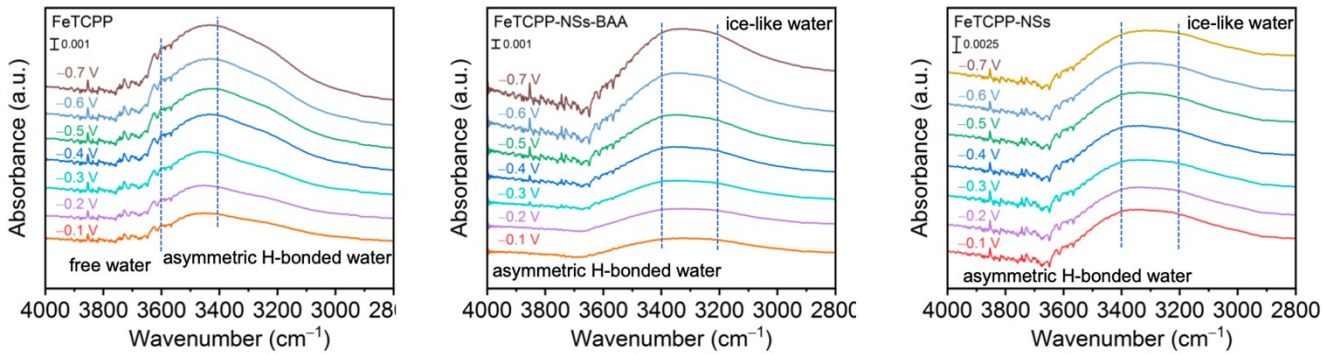

Fig. S26. Potential-dependent in situ ATR-SEIRAS spectra from –0.1 to –0.7 V.

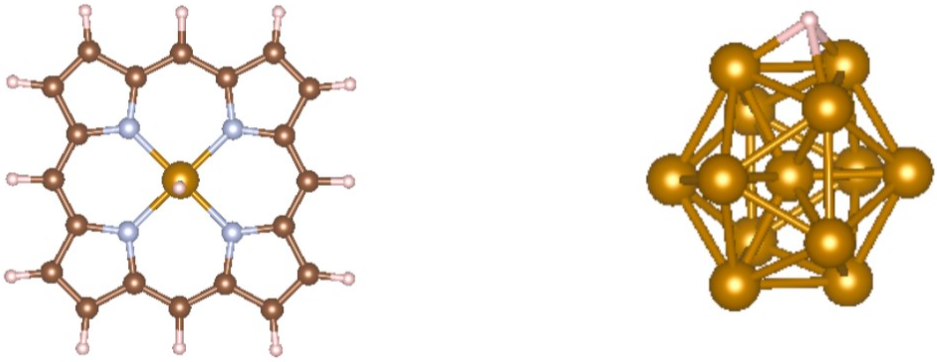

Fig. S27. The optimized adsorption model of *H on FeTCPP and Fe_{13} metal clusters.

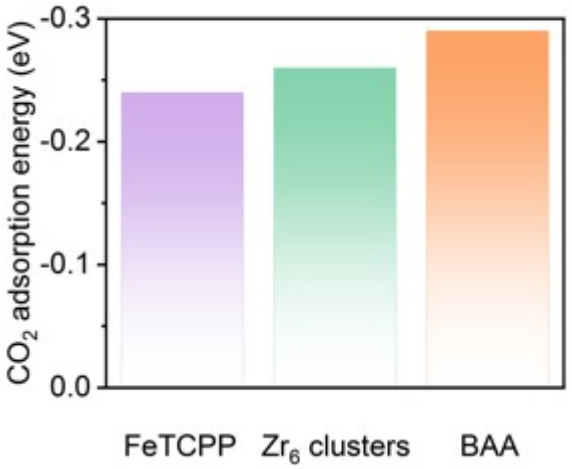

Fig. S28. The calculated ECO_2 values.

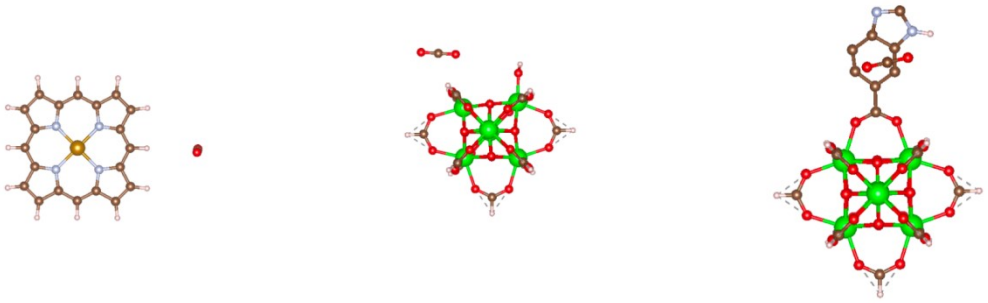

Fig. S29. The optimized adsorption model of CO_2 on FeTCPP, Zr_6 clusters, and BAA.

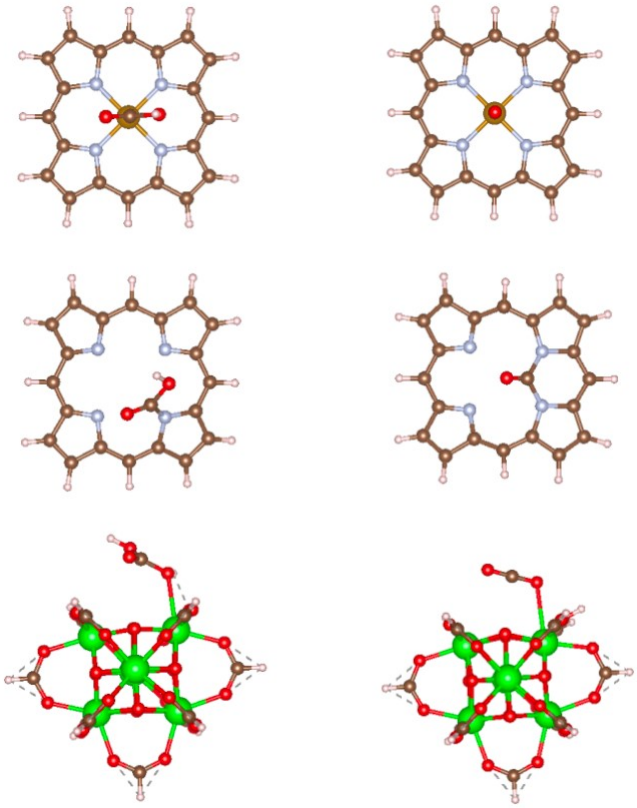

Fig. S30. The optimized adsorption model of COOH* and CO on FeTCPP, TCPP and Zr_6 clusters.

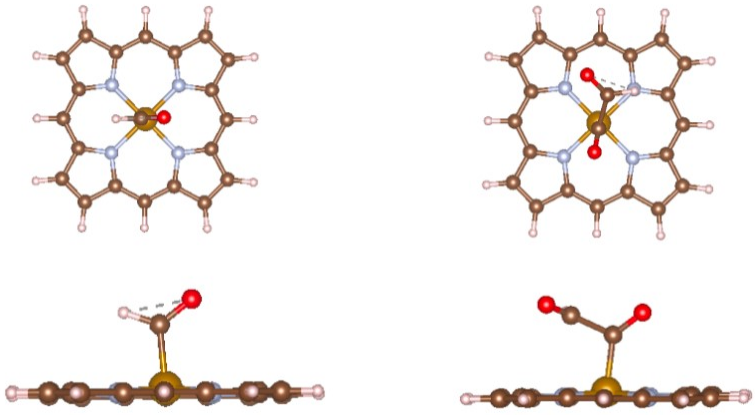

Fig. S31. The optimized adsorption model of *CHO and *OCCHO.

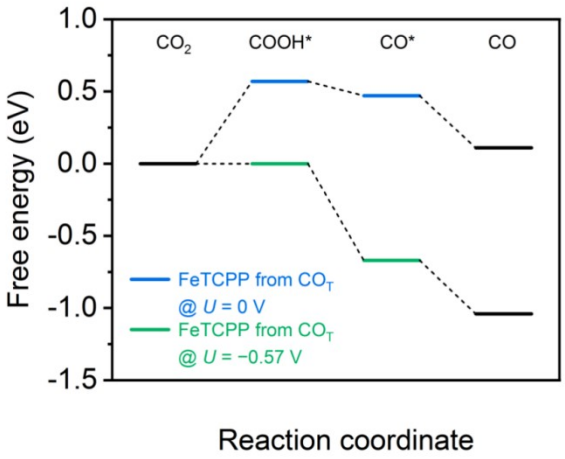

Fig. S32. Thermodynamic energy profiles for CO_2 to CO on FeTCPP via the $*CO_T$ pathway at different potentials.

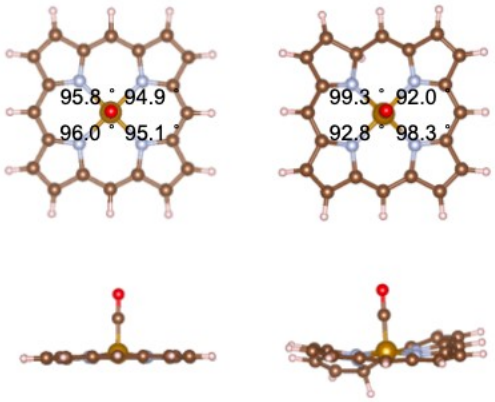

Fig. S33. The optimized adsorption model of *CO. To investigate the influence of potential on the structure of second-shell carbon atoms and the *CO adsorption structure, hydrogen atom was introduced to the second-shell carbon sites. By introducing addition electrons via adsorbed hydrogen atom to the FeTCPP structure, we simulated the structural changes of FeTCPP under negative potentials, particularly focusing on the variations in the second-shell carbon structure and the ∠N–Fe–C bond angle.

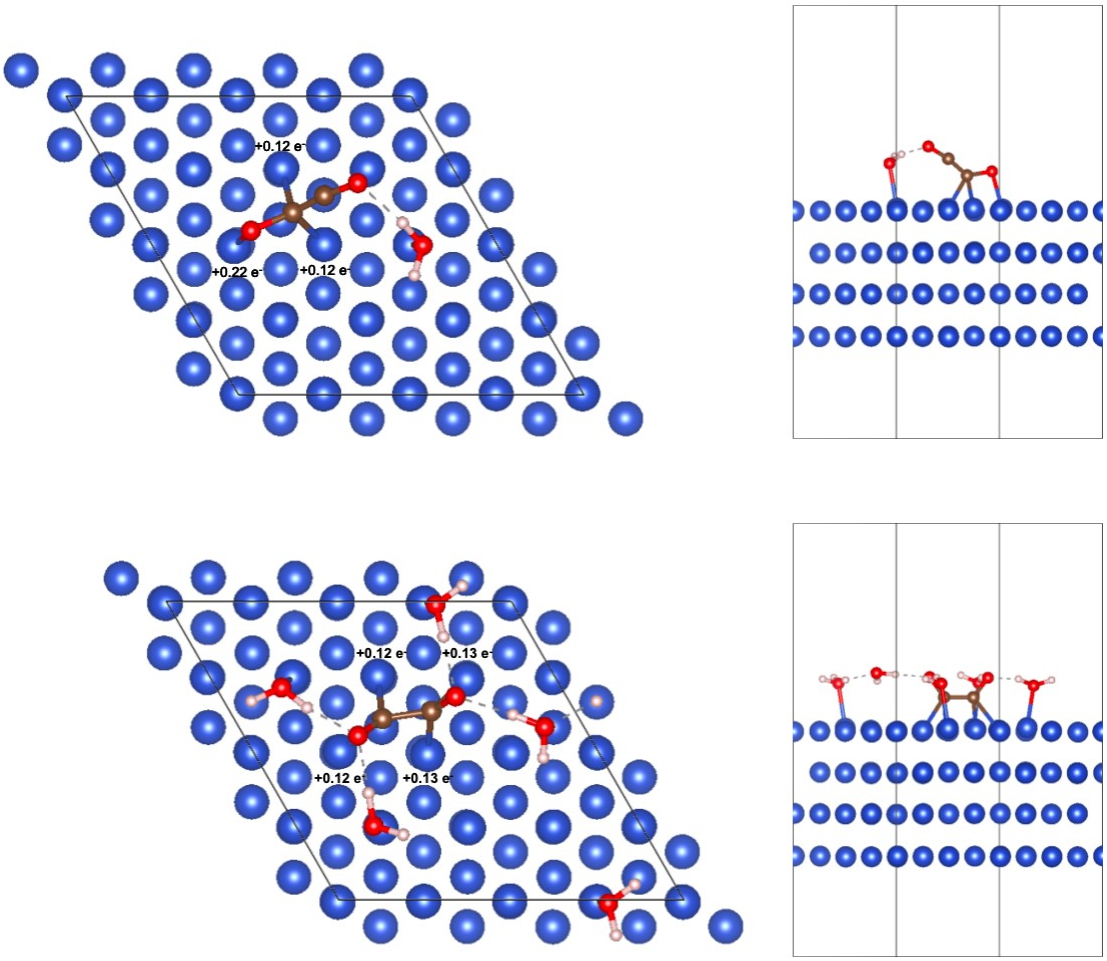

Fig. S34. The optimized adsorption model of *OCCO and H_2O on Cu (111) plane, along with the corresponding Bader charge analysis.

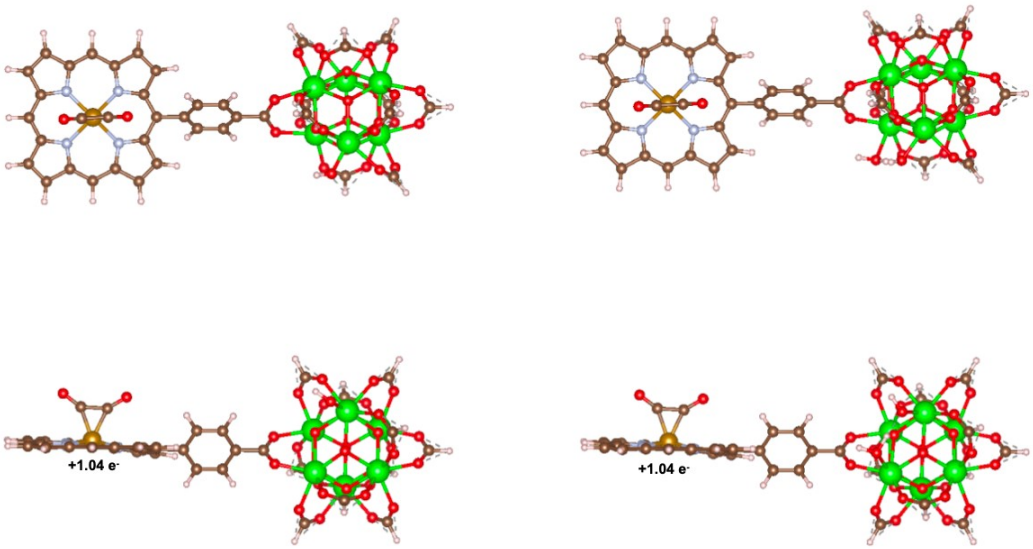

Fig. S35. The optimized adsorption model of *OCCO and H_2O on FeTCPP functionalized by Zr_6 clusters, along with the corresponding Bader charge analysis.

3. Electronic supplementary tables

Table R1. Rietveld refinement results of FeTCPP-NSs.

Chemical formula	$C_{102}O_{32}Zr_6H_{64}N_4Fe_1$
Crystal system	Triclinic
a (Å)	20.304 ± 0.014
b (Å)	19.962 ± 0.015
c (Å)	18.980 ± 0.006
alpha (degrees)	90.85 ± 0.05
beta (degrees)	91.93 ± 0.05
gamma (degrees)	118.72 ± 0.04
2θ range (degrees)	1-15
R_p	0.0668
R_{wp}	0.0910

Table S2. EXAFS fitting parameters at the Fe K-edge

Sample	Shell	[a]*CN*	[b]*R*(Å)	[c]σ^2	[d]ΔE_0 (eV)	*R* factor
FeTCPP-NSs-BAA	Fe-N	3.6 ± 0.2	2.02 ± 0.006	0.007 ± 0.001	2.66 ± 0.55	0.019
	Fe-C	7.3 ± 0.4	3.04 ± 0.002	0.005 ± 0.001		

[a]*CN*, coordination number; [b]*R*, distance between absorber and backscatter atoms; [c]σ^2, Debye-Waller factor to account for both thermal and structural disorders; [d]ΔE_0, inner potential correction; R factor indicates the goodness of the fit. $S0^2$ was fixed to 0.76, according to the experimental EXAFS fit of Fe foil by fixing CN as the known crystallographic value.

Table S3. Comparison of this work with previous studies on the electrocatalytic CO_2 to C_2H_5OH.

Materials	Type	Electrolyte	C_2H_5OH FE	Partial current density (mA cm^{-2})	Potential (RHE)	References
FeTCPP-NSs-BAA	H	0.1 M $KHCO_3$	79.8%	0.9	− 0.4 V	This work
	H	0.5 M K_2SO_4 pH = 3	89.2%	1.0	− 0.3 V	
	Flow	0.5 M K_2SO_4 pH = 3	83.3%	8.1	− 0.7 V	
PGA	H	0.5 M $KHCO_3$	48.7%	4.7	− 0.8 V	Adv. sci., 2022, 9, 2202006
c-NC	H	0.1 M $KHCO_3$	77%	< 0.25	− 0.56 V	Angew. Chem. Int. Ed., 2017, 56, 10840
B-NiO	Flow	0.1 M $KHCO_3$	75.2%	1.21	− 0.6 V	Adv. Mater., 2024, 36, 2410125
Br-FePc-F	H	0.1 M $KHCO_3$	34.3%	-	− 0.7 V	Adv. Funct. Mater., 2024, 34, 2402537
Ni@NCNT-700	H	0.5 M $KHCO_3$	38.5%	< 1	− 0.5 V	Carbon, 2023, 201, 460
Co-corrole	H	0.1 M $NaClO_4$ pH = 6.0	48%	< 2	− 0.8 V	Nat. Commun., 2019, 10, 3864
MC-CNT/Co	H	0.5 M $KHCO_3$	60.1%	~3	− 0.32 V	Chem. Sci., 2020, 11, 5098
BND	H	0.1 M $NaHCO_3$	93.2%	-	− 1.0 V	Angew. Chem. Int. Ed., 2017, 129, 15813
$Fe_2P_2S_6$	H	0.5 M $KHCO_3$	23.1%	< 0.1	− 0.2 V	ACS Catal., 2019, 9, 9721
MNC-5	H	0.1 M $KHCO_3$	78%	< 0.25	− 0.56 V	ChemSusChem, 2020, 13, 293
In_2S_3	H	0.1 M $KHCO_3$	44%	-	− 0.2 V	Chem. Eng. J., 2023, 475, 146456
FeP NA/TM	H	0.5 M $KHCO_3$	14.1%	< 0.2	− 0.2 V	Angew. Chem. Int. Ed., 2020, 56, 10840
hcp Co NSs	H	0.5 M $KHCO_3$	10%	-	− 0.5 V	J. Am. Chem. Soc., 2021, 143, 15335
RuPC/NPC	H	0.5 M $KHCO_3$	27.5%	-	− 0.64 V	Proc. Natl. Acad. Sci., 2019, 116, 26353
Cu-SACs-1 N-CQDs	H	0.1 M $KHCO_3$	70%	0.7	− 0.2 V	Appl. Catal. B Environ., 2024, 345, 123694
5-Ag/Cu_2O	H	0.1 M $KHCO_3$	17%	< 2	− 1.0 V	Angew. Chem. Int. Ed., 2021, 60, 7426
Hex-2Cu-O	H	0.1 M $KHCO_3$	32.5%	< 3.3	− 1.2 V	Nat. Commun., 2022, 13, 5122
Cu/$N_{0.14}C$	H	0.1 M $KHCO_3$	51%	14.4	− 1.1 V	Nat. Commun., 2022, 13, 5122
Cu/C-0.4	H	0.1 M $KHCO_3$	91%	< 2	− 0.7 V	Nat. Energy, 2022, 13, 1322

4. Electronic supplementary references

1. Ravel, B., Newville, M., Ravel, B. & Newville, M. ATHENA, ARTEMIS, HEPHAESTUS: data analysis for X-ray absorption spectroscopy using IFEFFIT. J. Synchrotron Radiat. 12, 537-541 (2005).
2. Knecht, M. R., Weir, M. G., Frenkel, A. I. & Crooks, R. M. Structural rearrangement of bimetallic alloy PdAu nanoparticles within dendrimer templates to yield core/shell configurations. Chem. Mater. 10, 1019-1028 (2008).
3. Kresse, G. & Furthmüller, J. Efficient iterative schemes for ab initio total-energy calculations using a plane-wave basis set. Phy. Rev. B 54, 11169-11186 (1996).
4. Perdew, J. P., Burke, K. & Ernzerhof, M. Generalized Gradient Approximation Made Simple. Phys. Rev. Lett. 77, 3865-3868 (1996).
5. Grimme, S., Antony, J., Ehrlich, S. & Krieg, H. A consistent and accurate ab initio parametrization of density functional dispersion correction (DFT-D) for the 94 elements H-Pu. J. Chem. Phys. 132, 154104 (2010).